

# The evolving Glasma

Kenji Fukushima<sup>a</sup> and François Gelis<sup>b</sup>

<sup>a</sup>*Department of Physics, Keio University, Kanagawa 223-8522, Japan*

<sup>b</sup>*Institut de Physique Théorique (URA 2306 du CNRS) CEA/DSM/Saclay,  
91191, Gif-sur-Yvette Cedex, France*

---

## Abstract

We extensively study the growing behavior of the energy and the pressure components depending on the space-time rapidity in the framework of the Glasma, which describes the early-time dynamics in the ultra-relativistic heavy-ion collisions. We simulate the Glasma solving the classical equations of motion in the SU(2) Yang-Mills theory and systematically investigate the dependence of the Glasma instability on the model parameters. We have checked that the transverse and longitudinal grid sizes in our simulation are large enough to handle cutoff effects under control. By comparing the numerical results from several initial conditions with different magnitudes of instability seed and also those with different wave-numbers for rapidity fluctuations, we clearly see that unstable modes dominantly grow up in the linear regime and we also confirm non-linear effects in the time evolution. To extract more detailed information on the evolving Glasma, we decompose the energy into the components in terms of rapidity wave-numbers. We observe an energy flow from low wave-number modes into higher wave-number modes due to non-linearity in the equations of motion. We find that the energy spectrum approaches an asymptotic scaling that is consistent with Kolmogorov's power-law form even in the expanding system of the Glasma.

*Key words:* Color Glass Condensate, Glasma, Relativistic heavy-ion collision, Instability, Kolmogorov spectrum

---

## 1 Introduction

The formation of a quark-gluon plasma (QGP) is achieved in ultra-relativistic heavy-ion collision experiments at Relativistic Heavy-Ion Collider (RHIC) in BNL and at the Large Hadron Collider (LHC) in CERN. More and more information on properties of strongly interacting quark-gluon matter in quantum chromodynamics (QCD) is being accumulated. However, despite a number of

interesting discoveries and new notions established in experiments, the thermalization mechanism that leads to the QGP still lacks a deep understanding based on QCD first principles.

There have been many attempts to estimate the thermalization time scale, that is phenomenologically known to be  $\tau_{\text{eq}} \lesssim 1 \text{ fm}/c$  from analysis in hydrodynamic models [1,2]. It was argued [3] that perturbative QCD processes lead to a thermalization time of order  $\alpha^{-13/5} Q_s^{-1}$  where the saturation momentum  $Q_s$  is a characteristic hard scale in the high-energy reactions;  $Q_s(x \sim p_\perp/\sqrt{s}) = 1\text{--}2 \text{ GeV}$  in the typical RHIC kinematics. If the prefactor is of order unity, this estimate would yield a thermalization time around several fm/c, which is too slow to account for the RHIC observations. It has also been suggested that QCD perturbation theory, no matter at which order one truncates it, may be unable to describe thermalization at all [4]. Plasma instabilities, particularly the Weibel instability [5,6,7,8,9,10,11,12], could be promising candidates for the early thermalization mechanism [13] and have been well investigated in the hard-loop formalism [14,15,16,17,18]. There are also various other approaches [19,20,21,22] including a framework based on the AdS/CFT correspondence [23,24,25,26], in which thermalization appears as the formation of a black hole horizon in the dual theory.

Parallel to the analysis on plasma instabilities, an important observation was made in a related theoretical framework. The occupation number of gluons at high energy is so huge that color field amplitudes  $A^\mu \sim \alpha_s^{-1/2}$  can be realized, and then non-linearities must be taken into account to all orders. Instead of a plain perturbative expansion, then, an approximation in terms of classical field equations becomes more suitable because it effectively makes a resummation of large-amplitude fields  $A_\mu$ . This non-linear regime, whose natural time scale is of order  $Q_s^{-1} \simeq 0.2 \text{ fm}/c$  at RHIC, is expected to be prevalent during the early stages in heavy-ion collisions. The QCD framework known as the Color Glass Condensate (CGC) [27,28] rearranges the perturbative expansion in terms of classical fields (that correspond to the resummation of infinite sets of graphs), and perturbations on top of these classical fields are of higher order in  $\alpha_s$ . The CGC was first developed in order to deal with the saturation effect in the gluon distribution function [29,30,31]. Because we are interested in the early time ( $\tau \lesssim Q_s^{-1}$ ) dynamics before thermalization, the CGC description seems to be the most suited for our purpose. The initial condition just above the forward light-cone (i.e. at  $\tau = 0^+$ ) for the classical field that appears at lowest order in the CGC description can be nicely formulated in the Bjorken (expanding) coordinates [32,33]. Because in the regime of large occupation numbers, classical field theory and kinetic theory essentially describe the same dynamics [34,35], it is conceivable that the CGC can describe the isotropization and thermalization processes qualitatively. However, for this program to have a chance to work, it is necessary to go beyond the lowest order description, since at zeroth order it is well known that the pressure tensor

never isotropizes.

It is unfortunately impossible to obtain an analytical solution of the classical Yang-Mills equations of motion for the heavy-ion collision (two-source) problem, and therefore one has to resort to numerical simulations. In Refs. [36,37,38], heavy-ion collisions were simulated in the McLerran-Venugopalan (MV) model (i.e. the CGC at lowest order, with a local Gaussian distribution of color sources), formulated gauge-invariantly in terms of link variables. These numerical calculations were later confirmed by an independent simulation in Ref. [39]. The peculiar feature in the CGC description at leading order is that the initial condition for the classical fields is independent of the space-time rapidity variable  $\eta$ , and the equations of motion maintain  $\eta$ -independence during the time evolution. Therefore, the space-time evolution is entirely independent of  $\eta$ , that is, invariant under boosts in the direction of the collision axis. Intuitively, one can expect a longitudinally extended structure of the initial fields, which is indeed a characteristic property of the so-called “Glasma” state [40], which could be a source for the so-called ridge structure seen in the two-particle correlations at RHIC and LHC [41,42].

Within the CGC framework, an instability has been found when the boost invariant Glasma fields are disturbed [43,44]. This instability has some similarities to the Weibel instability in anisotropic plasmas, but the origin of the instability is not yet fully clarified, though several interpretations have been proposed [45,46,47,48,49]. Also, it is still an issue how to properly formulate disturbances to the boost invariant CGC background. However, it is clear that such perturbations arise when one considers higher order corrections to the leading CGC picture [50], and therefore they should not be ignored since they can alter phenomena such as particle production [51,52,53], etc. Moreover, without including these perturbations, one cannot quantify the thermalization processes.

One of the reasons why the origin of the Glasma instability lacks a clear understanding is that the available numerical data from earlier works [43,44] is rather limited. This motivates us to carry out a more systematic survey of the Glasma instability, exploiting a wider range of simulation parameters. In this work we will specifically investigate the dependence of the Glasma instability on the following parameters:

[i] *Transverse grid size  $N$* : It is known that the initial energy density at  $\tau = 0^+$  is sensitive to the ultraviolet and infrared regulators in the transverse direction, and this sensitivity becomes milder at finite  $\tau$  [4,45,54]. It is therefore important to check whether continuum-limit results can be obtained reliably by looking systematically at the dependence on the transverse lattice spacing  $a \equiv L/N$ , where  $L$  is the length of the box and  $N$  the number of lattice points in the transverse direction.

[ii] *Longitudinal grid size  $N_\eta$* : Physical results should also not be contaminated by ultraviolet singularities in the longitudinal direction. To avoid this, we will use initial fluctuations with sufficiently small longitudinal wave-number  $\nu$  ( $\nu$  is the Fourier conjugate to the rapidity  $\eta$ ). We will confirm that there is no dependence on the longitudinal grid size  $N_\eta$  or the longitudinal lattice spacing  $a_\eta \equiv L_\eta/N_\eta$ , at least until the longitudinal spectrum extends into the ultraviolet regions at very late time.

[iii] *Magnitude  $\Delta$  of the seeds*: In general the strength of the instability increases with the magnitude  $\Delta$  of the initial  $\eta$ -dependent perturbations. This dependence is found to be very simple until the unstable modes become large enough to be self-interacting: at moderate times, the finite- $\nu$  modes obey the linearized dynamics and their amplitudes grow linearly as  $\Delta$  increases.

[iv] *Initial wave-number  $\nu_0$* : The time evolution depends on the initial condition in the longitudinal direction, and in particular on the wave-number  $\nu_0$  of the seeds. We will show that the instability produced by the smallest wave-number<sup>1</sup> ( $\nu_0 = \pm 1$ ) is the fastest and strongest in a wide range of times. We will also confirm the dominance of linearity and the appreciable presence of residual non-linear effects by verifying that the result from an initial condition with multiple  $\nu_0$ 's can be approximated as the superposition of the results from initial conditions with single wave-numbers  $\nu_0$ 's.

In this paper, we report on numerical results about these dependences for the growing behavior at the late stage of the Glasma evolution. These numerical results provide a pool of observations that we hope will help to understand the microscopic mechanisms that drive the Glasma instabilities. In the section 2, we recall the most important formulas for a lattice study of this problem. In the section 3, we briefly expose some results in the purely boost-invariant case. These are well-known results already, and merely serve as a check of our implementation. In the section 4, we describe what happens when the Glasma fields are perturbed by a rapidity-dependent seed, and we investigate thoroughly how the result depends on the parameters listed above. We explore the time evolution of the  $\nu$ -spectrum in the section 5. Finally, the section 6 is devoted to a summary and outlook.

## 2 Lattice formulation of the problem

In this section, we summarize our equations, with emphasis on the lattice specificities. The main goal of this section is to avoid confusions due to the

---

<sup>1</sup> In our conventions, the wave-number  $\nu$  is defined to be an integer between  $-N_\eta/2$  and  $+N_\eta/2$ . The lowest non-zero wave-number is thus  $\nu = \pm 1$ .

existence of different conventions in the literature for some quantities.

The link variables are defined as  $U_\mu(x) \equiv e^{-igaA_\mu(x)}$  with the gauge potential  $A_\mu(x)$  that connects the neighboring sites from  $x$  and  $x + \hat{\mu}$ . This expression for the link variable is the most important one in order to establish the correspondence between the continuum and the lattice (link-variable) formulations. Under a gauge transformation by  $V(x)$  the link variables transform as

$$U_\mu(x) \rightarrow V(x)U_\mu(x)V^\dagger(x + \hat{\mu}) , \quad (1)$$

and the chromo-electric fields as

$$E^i(x) \rightarrow V(x)E^i(x)V^\dagger(x) . \quad (2)$$

The plaquette variable is then defined as

$$U_{\mu\nu}(x) \equiv U_\mu(x)U_\nu(x + \hat{\mu})U_\mu^\dagger(x + \hat{\nu})U_\nu^\dagger(x) \approx \exp[-iga^2F_{\mu\nu}(x)] , \quad (3)$$

where the last form is an approximation which gives rise to the field strength  $F_{\mu\nu} \equiv \partial_\mu A_\nu - \partial_\nu A_\mu - ig[A_\mu, A_\nu]$  of the continuum formulation. This is a very useful expression to study the continuum limit. The lattice spacing should be the longitudinal one, i.e.  $a_\eta$ , which is distinct from the transverse one  $a$ , if the longitudinal direction is involved in the displacements  $\hat{\mu}$  or  $\hat{\nu}$  in the above formula. The canonical momenta in terms of link variables are expressed as

$$\partial_\tau U_i(x) = \frac{-ig}{\tau} E^i(x)U_i(x) , \quad \partial_\tau U_\eta(x) = -iga_\eta\tau E^\eta(x)U_\eta(x) . \quad (4)$$

Here we note that in the above we already use variables made dimensionless by the transverse lattice spacing  $a$ , and thus  $a$  will never appear explicitly in our formula. Because  $\eta$  is a dimensionless number,  $a_\eta$  does not bring any mass dimension unlike  $a$ .

We can also discretize the time in the above equations in order to solve the time evolution numerically for  $U_i(x)$  and  $U_\eta(x)$ ;

$$U_i(\tau'') = \exp[-2\Delta\tau \cdot igE^i(\tau')/\tau']U_i(\tau) , \quad (5)$$

$$U_\eta(\tau'') = \exp[-2\Delta\tau \cdot ig a_\eta \tau' E^\eta(\tau')]U_\eta(\tau) , \quad (6)$$

where  $\tau' = \tau + \Delta\tau$  and  $\tau'' = \tau + 2\Delta$ . Note that we have not written explicitly the position arguments in the quantities that appear in these equations. Here, the exponentiation of  $E^\mu$  is important; otherwise the updated  $U_\mu(\tau'')$  would not be a unitary matrix. The equations of motion are discretized in the same

manner as

$$E^i(\tau') = E^i(\tau - \Delta\tau) + 2\Delta\tau \frac{i}{2ga_\eta^2\tau} \left[ U_{\eta i}(x) + U_{-\eta i}(x) - (\text{h.c.}) \right]_\tau \\ + 2\Delta\tau \frac{i\tau}{2g} \sum_{j \neq i} \left[ U_{ji}(x) + U_{-ji}(x) - (\text{h.c.}) \right]_\tau, \quad (7)$$

for the transverse components and

$$E^\eta(\tau') = E^\eta(\tau - \Delta\tau) + 2\Delta\tau \frac{i}{2ga_\eta\tau} \sum_{j=x,y} \left[ U_{j\eta}(x) + U_{-j\eta}(x) - (\text{h.c.}) \right]_\tau, \quad (8)$$

for the longitudinal component. We recall again that all variables including  $\tau$  and  $\Delta\tau$  above are dimensionless, and expressed in unit of the transverse spacing  $a$ . One can make sure that these equations are equivalent to the ordinary equations of motion in the continuum limit, by using the approximate form (3).

The initial conditions are derived from the requirement of avoiding the singularity at the collision point. It is written in terms of  $U_i^{(m)}$ , the classical solution of the MV model for a single color source (the label  $m = 1, 2$  indicates which of the two nuclei produces the corresponding field). This single-source classical solution is a transverse pure-gauge,

$$U_i^{(m)}(\mathbf{x}_\perp) = V^{(m)}(\mathbf{x}_\perp) V^{(m)\dagger}(\mathbf{x}_\perp + \Delta\mathbf{x}_i), \quad (9)$$

where the gauge rotation matrix  $V^{(m)}$  can be written as

$$V^{(m)\dagger}(\mathbf{x}_\perp) = \exp \left[ ig\Lambda^{(m)}(\mathbf{x}_\perp) \right]. \quad (10)$$

Here,  $\Lambda^{(m)}$  is the solution of the Poisson equation,  $\partial_\perp^2 \Lambda^{(m)}(\mathbf{x}_\perp) = -\rho^{(m)}(\mathbf{x}_\perp)$ . In the MV model, the random color source  $\rho^{(m)}$  is Gaussian distributed<sup>2</sup>, with a two-point correlation

$$\langle \rho^{(n)}(\mathbf{x}_\perp) \rho^{(m)}(\mathbf{x}'_\perp) \rangle = \delta^{nm} g^2 \mu^2 \delta(\mathbf{x}_\perp - \mathbf{x}'_\perp). \quad (11)$$

Higher-point correlation functions are obtained as products of two-point contractions, via Wick's theorem. In the MV model,  $\mu$  is the only dimensionful parameter and it is related to the saturation momentum  $Q_s$ . Then, the initial

---

<sup>2</sup> A Gaussian distribution, albeit one with non-local correlations, is also an approximate solution of the JIMWLK evolution equation [55].

conditions are [36];

$$U_i = \left( U_i^{(1)} + U_i^{(2)} \right) \left( U_i^{(1)\dagger} + U_i^{(2)\dagger} \right)^{-1} , \quad (12)$$

$$E^\eta = \frac{-i}{4g} \sum_{i=x,y} \left[ \left( U_i - 1 \right) \left( U_i^{(2)\dagger} - U_i^{(1)\dagger} \right) + \left( U_i^\dagger(x - \Delta x_i) - 1 \right) \left( U_i^{(2)\dagger}(x - \Delta x_i) - U_i^{(1)\dagger}(x - \Delta x_i) \right) - (\text{h.c.}) \right] , \quad (13)$$

written here in the slightly simpler case of the SU(2) color group. These discretized equations of motion and initial conditions completely define the numerical MV model. Our conventions are mostly consistent with those of previous works, except for the fact that the field  $A_\eta$  is not treated as an adjoint scalar-field variable but instead we also describe it in terms of a link variable  $U_\eta$ . We note that our formulation is reduced to the conventional one with the adjoint scalar-field variable if we take  $a_\eta$  to be sufficiently small. In addition, since our interest lies primarily in the qualitative behavior of the Glasma instability, we disregard the color neutralization that has been imposed onto the MV model color sources in other works [56,57].

It is now straightforward to implement the numerical calculation for gauge-invariant observables such as the components of the energy-momentum tensor. They are in the continuum convention written down as

$$\varepsilon = \langle T^{\tau\tau} \rangle = \langle \text{tr} [E_L^2 + B_L^2 + E_T^2 + B_T^2] \rangle , \quad (14)$$

$$P_T = \frac{1}{2} \langle T^{xx} + T^{yy} \rangle = \langle \text{tr} [E_L^2 + B_L^2] \rangle , \quad (15)$$

$$P_L = \langle \tau^2 T^{\eta\eta} \rangle = \langle \text{tr} [E_T^2 + B_T^2 - E_L^2 - B_L^2] \rangle , \quad (16)$$

where we define

$$E_L^2 \equiv E^{\eta a} E^{\eta a} , \quad E_T^2 \equiv \frac{1}{\tau^2} \left( E^{xa} E^{xa} + E^{ya} E^{ya} \right) . \quad (17)$$

These formulas are implicitly summed over the color index  $a$ , for  $E_L^2$  and  $E_T^2$  to be gauge invariant. Here, the chromo-magnetic field squared should be expressed in a way consistent with Eq. (3), that is,

$$B_L^2 = \frac{2}{g^2} \text{tr} (1 - U_{xy}) , \quad B_T^2 = \frac{2}{(ga_\eta\tau)^2} \sum_{i=x,y} \text{tr} (1 - U_{\eta i}) . \quad (18)$$

These definitions are, however, not very convenient when we decompose the energy into its Fourier components, as we will see later. We confirm that the energy-momentum tensor is traceless;  $T^\mu{}_\mu = T^{\tau\tau} - T^{xx} - T^{yy} - \tau^2 T^{\eta\eta} = 0$ . It should also be mentioned that our definition of  $P_T$  is different from that in Refs. [43,44] by a factor 2 so that  $P_T = P_L$  for an isotropic system.

### 3 Boost Invariant Expansion

We first check the consistency with the known results in the boost-invariant case, i.e. in  $(2 + 1)$  dimensions. This is useful also for later discussions on the spectral decomposition when we consider  $\eta$ -dependent fluctuations. In this section, we focus on  $\eta$ -independent classical solutions, with initial conditions specified in Eqs. (12) and (13) that are themselves independent of  $\eta$ . Eventually, however, our goal is to superimpose  $\eta$ -dependent fluctuations to these boost invariant initial conditions in order to incorporate quantum effects [50].

We note here that our numerical calculations are limited to the  $SU(2)$  color group, so that we can get more samples and thus better statistics for the same computational cost. As discussed in Ref. [18], the  $SU(2)$  calculations capture the essential properties of the Glasma instability, and we expect that the results we report here for the  $SU(2)$  case would be qualitatively the same for  $SU(3)$ .

#### 3.1 Initial Configurations

Let us first take a look at a typical fixed initial configuration, without taking the ensemble average over the color sources, in order to develop an intuitive picture for the Glasma state. In the MV model, the initial color distribution in the transverse plane is akin to white noise, having no correlation between different transverse sites<sup>3</sup>. Since the solution of the Poisson equation  $\partial_{\perp}^2 \Lambda^{(m)}(\mathbf{x}_{\perp}) = -\rho^{(m)}(\mathbf{x}_{\perp})$  involves a convolution with a massless (i.e. long ranged) transverse propagator,  $\Lambda(\mathbf{x}_{\perp})$  has a smooth structure as shown in the left panel of Fig. 1.

Although  $\Lambda(\mathbf{x}_{\perp})$  is fairly smooth due to the regularizing effect of this convolution, the corresponding gauge field  $\alpha_i(\mathbf{x}_{\perp})$ , which is a phase of  $U_i(\mathbf{x}_{\perp})$  defined in Eq. (9), is far from smooth. This is actually a consequence of the pure-gauge form; contributions from globally smooth parts in  $\Lambda(\mathbf{x}_{\perp})$  cancel each other and the resulting  $\alpha_i(\mathbf{x}_{\perp})$  fluctuates strongly. In other words,  $\alpha_i(\mathbf{x}_{\perp})$  has a rough structure because a derivative of  $\Lambda(\mathbf{x}_{\perp})$  undoes the regularization provided by the convolution. The  $\alpha_i(\mathbf{x}_{\perp})$  shown in the figure 1 is the gauge field from a single source only. In a collision, the initial fields such as  $E^{\eta}(\mathbf{x}_{\perp})$

---

<sup>3</sup> This property would be slightly altered if one imposed to the color distribution to be color neutral over patches corresponding to the size of a nucleon, or if one were using distributions of sources evolved with the JIMWLK equation – in the latter case, it has been shown that the JIMWLK evolutions induces correlations among the sources over transverse distances of the order of  $Q_s^{-1}$ .



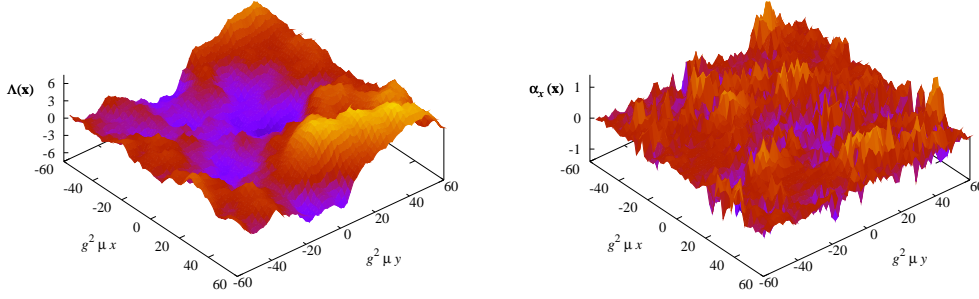


Fig. 1. An initial configuration generated by a random color source  $\rho(\mathbf{x}_\perp)$ . The MV-model parameters are chosen as  $N = 64$  (number of transverse sites) and  $g^2\mu L = 120$ . Left: The solution  $\Lambda(\mathbf{x}_\perp)$  of the Poisson equation. Only the first color component  $\Lambda^1(\mathbf{x}_\perp)$  is plotted. Right: Corresponding gauge field  $\alpha_x(\mathbf{x}_\perp)$  calculated from  $e^{-ig\Lambda(\mathbf{x}_\perp)}e^{ig\Lambda(\mathbf{x}_\perp+i)} = \exp[-ig\alpha_i(\mathbf{x}_\perp)]$ . Only the first color component  $\alpha_x^1(\mathbf{x}_\perp)$  is plotted.

and  $B^\eta(\mathbf{x}_\perp)$  involve a product of two  $\alpha_i(\mathbf{x}_\perp)$ 's from two independent sources, and thus have an even rougher structure.

It is worth mentioning that the “color-flux tube” structures, whose transverse size is expected to be of order  $Q_s^{-1}$ , do not emerge manifestly from the MV model since the source distribution has no correlation length in the transverse direction. This means that the Nielsen-Olesen instability [48] is unlikely to occur at least within the MV model. Nevertheless, we expect that color-flux tube structures would appear after the JIMWLK evolution from the MV-model distribution. In the mean-field approximation, in fact, the transverse correlation function of color source has been already studied in Ref. [55], which should be taken into account in the future works. Also, to make a clear comparison with the Weibel instability and the hard-loop estimates (especially early works [14,15]), it would be useful to simplify the MV-model setup in (1+1) dimensions without transverse dependences in such a way not to lose the qualitative features of the Glasma instability that we will see in the section 4. In this sense the results reported in the present paper should serve as a foundation for future investigations in these directions.

### 3.2 Time Evolution

Figure 2 shows the time evolution of the energy density (17) and (18). We set  $g^2\mu L = 120$  which means that  $g^2\mu R_A = 67.7$  with  $\pi R_A^2 = L^2$  according to the convention for the RHIC physics in the literature [39]. This choice corresponds to  $R_A \approx 7$  fm [ $\simeq 1.2 \times (197)^{1/3}$  fm (i.e. the radius of the Au atom)] and  $g^2\mu \approx 2$  GeV (where  $g = 2$  as usually chosen, meaning that  $\alpha_s \simeq 0.3$ ). In most of the numerical results presented in this work, we keep

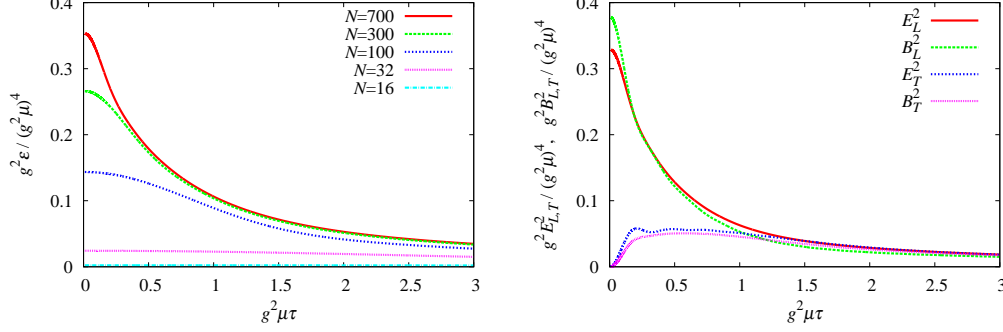


Fig. 2. Left: Energy density (14) for various choices of the transverse grid size  $N$ . An ensemble average is taken over 30 random configurations of  $\rho^{(m)}(\mathbf{x}_\perp)$  for  $N = 700$  and 300, and over 50 configurations for  $N = 100, 32, 16$  and 8. The MV model parameter is chosen as  $g^2\mu L = 120$ . Right: Chromo-electric and chromo-magnetic fields (17) and (18) for the same MV model parameters and  $N = 700$ .

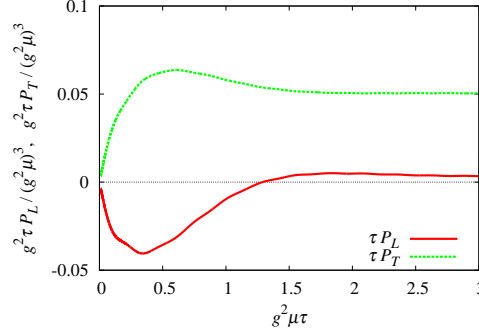


Fig. 3. Longitudinal pressure  $P_L$  defined in Eq. (16) and transverse pressure  $P_T$  defined in Eq. (15), multiplied by  $g^2\mu\tau$ .

using these parameters. We note that the strength of the Glasma instability as seen in the next section is set by the instability seed  $\Delta$  relative to  $g^2\mu$  which characterizes the CGC background. In this sense, for our purpose in later discussions, the precise value of  $g^2\mu L$  is of no qualitative importance.

In Fig. 2, we investigate the dependence on the transverse grid size  $N$ : The left plot shows how the energy density increases with increasing  $N$ , varying from  $N = 8$  to  $N = 700$  from the bottom curve to the topmost one. It is already known in the literature [39] that the  $N$ -dependence (or the UV-cut-off dependence) is significant at  $g^2\mu\tau \ll 1$ , but becomes almost irrelevant for  $g^2\mu\tau \gtrsim 1$  (except for small lattice sizes  $N \ll 100$ ).

As is well-known from earlier works [36,37], the energy density decreases as  $\tau^{-1}$ , which is the scaling behavior of a free-streaming expansion. In fact the energy density multiplied by the time,  $\tau\epsilon$ , saturates at a time  $g^2\mu\tau \simeq 1$  (which is sometimes called the formation time, i.e. the time at which partons are freed from the wave-function of the nuclei) where the free-streaming expansion

starts. This is natural on physical grounds, because the classical fields keep interacting strongly until  $g^2\mu\tau \simeq 1$ , and become quasi-free at  $g^2\mu\tau \gg 1$ .

We see that the longitudinal chromo-electric and chromo-magnetic fields behave in the same way, which is the characteristic feature of the Glasma initial state [40]. In our convention  $E_L^2$ ,  $B_L^2$ ,  $E_T^2$ , and  $B_T^2$  are all approaching a common value for  $g^2\mu\tau > 1$ , and the system still remains anisotropic (isotropy requires that  $E_T^2 = 2E_L^2$  and  $B_T^2 = 2B_L^2$ ). This becomes clearer if we consider the transverse pressure  $P_T$  and the longitudinal one  $P_L$  defined in Eqs. (15) and (16), respectively, as shown in Fig. 3. Then, we can find that  $\tau P_T$  and  $\tau P_L$  both approach an asymptotic value and  $\tau P_L$  is much smaller than  $\tau P_T$ . If  $P_L$  is exactly zero, this means that the system reaches the limit of the free-streaming expansion leading to  $\varepsilon \propto \tau^{-1}$ . If the system is completely thermalized, on the other hand, the pressure must be isotropic and thus  $P_T = P_L$ . Because an expansion with positive  $P_L$  produces work against the expansion of the matter, the energy density decreases faster than in the free-streaming case, e.g.  $\varepsilon \propto \tau^{-4/3}$  if  $P_L = \varepsilon/3$  and if the expansion is purely longitudinal (i.e. Bjorken expansion). Therefore, the (leading order) Glasma state alone cannot reach isotropization; a candidate for causing the longitudinal pressure to grow is the instability due to the  $\eta$ -dependent fluctuations that occur in higher order corrections.

### 3.3 Spectral Decomposition

Let us now consider the time evolution of the spectral composition of the energy content. That is, the energy is written in terms of Fourier components as

$$\varepsilon_E = \int \frac{d^2k_\perp}{(2\pi)^2} \varepsilon_E(k_\perp), \quad \varepsilon_B = \int \frac{d^2k_\perp}{(2\pi)^2} \varepsilon_B(k_\perp) \quad (19)$$

in terms of the continuum variables. If written in terms of the lattice variables, the transverse momenta take discrete values  $k_i = 2\pi n_i/L$  and the integration is replaced by a summation over  $n_i$ . The energy density in the mode  $k_\perp$  is given by

$$\varepsilon_E(k_\perp) \equiv \left\langle \text{tr} \left[ E^{\eta a}(-\mathbf{k}_\perp) E^{\eta a}(\mathbf{k}_\perp) + \tau^{-2} \left( E^{ia}(-\mathbf{k}_\perp) E^{ia}(\mathbf{k}_\perp) \right) \right] \right\rangle, \quad (20)$$

$$\varepsilon_B(k_\perp) \equiv \left\langle \text{tr} \left[ B^{\eta a}(-\mathbf{k}_\perp) B^{\eta a}(\mathbf{k}_\perp) + \tau^{-2} \left( B^{ia}(-\mathbf{k}_\perp) B^{ia}(\mathbf{k}_\perp) \right) \right] \right\rangle, \quad (21)$$

where  $E^{\eta a}(\mathbf{k}_\perp)$ ,  $E^{ia}(\mathbf{k}_\perp)$ ,  $B^{\eta a}(\mathbf{k}_\perp)$ , and  $B^{ia}(\mathbf{k}_\perp)$  are the Fourier transforms of the chromo-electric and chromo-magnetic fields. The above expressions are given in terms of the continuum variables, but it is non-trivial how to re-express them in terms of the link variables: Equation (20) for the chromo-

electric component is not changed, but we cannot use Eq. (21) as it is<sup>4</sup>.

It is of course possible to introduce the chromo-magnetic field using the relation (3) in such a way that

$$\begin{aligned} B_L^a &= F_{xy}^a \approx \frac{2}{ig} \text{tr} [t^a (1 - U_{xy})] \\ B_x^a &= F_{\eta y}^a \approx \frac{2}{iga_\eta} \text{tr} [t^a (1 - U_{\eta y})], \quad B_y^a = F_{\eta x}^a \approx \frac{2}{iga_\eta} \text{tr} [t^a (1 - U_{\eta x})]. \end{aligned} \quad (22)$$

This approximation works for sufficiently large number of the transverse sites, i.e.  $N \gtrsim 100$ . Then, we in principle have two options here: we abandon the information on  $\varepsilon_B(k_\perp)$  and just evaluate  $\varepsilon_E(k_\perp)$  to see the spectral pattern, or, we adopt a sufficiently large value of  $N$  so that we can use the approximation (22). In this work we take the former option, because simulations with  $N \gtrsim 100$  would be too time-consuming in the forthcoming studies that include  $\eta$ -dependent fluctuations (and where one thus needs to solve  $(3+1)$  dimensional equations).

At  $\tau = 0$ , the initial spectrum is calculable analytically in the MV model, leading to the expression [58],

$$\varepsilon = \frac{3(g^2\mu)^4}{2\pi g^2} \int \frac{d^2\mathbf{k}_\perp}{(2\pi)^2} \frac{1}{k_\perp \sqrt{k_\perp^2 + 4m^2}} \ln \left[ \frac{\sqrt{k_\perp^2 + 4m^2} + k_\perp}{\sqrt{k_\perp^2 + 4m^2} - k_\perp} \right], \quad (23)$$

with an IR cutoff  $m$ . This formula means that  $\varepsilon_E(k_\perp)$  behaves as  $k_\perp^{-2} \ln(k_\perp/m)$  at large  $k_\perp$ , which is the expected perturbative tail.

At non-zero  $\tau$ , we have evaluated  $\varepsilon_E(k_\perp)$  numerically, with results shown in Fig. 4. To draw the figure, we have calculated  $\varepsilon_E(k_\perp = \sqrt{k_x^2 + k_y^2})$  first as a function of  $k_x = 2\pi n_x/L$  and  $k_y = 2\pi n_y/L$  and then have taken an average over the results that lie in a bin,  $N < \sqrt{n_x^2 + n_y^2} < N + 1$ , to obtain  $\varepsilon_E(k_\perp)$  with  $k_\perp = 2\pi N/L$ . We use logarithmic horizontal and vertical axes in the plot of Fig. 4, to facilitate the identification of the initial-time power-law scaling in the spectrum.

We can notice that the energy spectrum at the initial time  $g^2\mu\tau = 0.01$  (where we started the simulation) obeys the perturbative scaling  $\sim k_\perp^{-2}$  up to the UV-cutoff, as indicated by a line for eye guide in Fig. 4 – in agreement with the perturbative expression in Eq. (23). The spectral shape quickly approaches

---

<sup>4</sup> This is an issue only because we want to decompose the magnetic energy in Fourier modes. If we stay in configuration space, the expressions for  $B_L^2$  and  $B_T^2$  in Eq. (18) are perfectly fine to calculate the chromo-magnetic energy – the problem is that they are not simply a sum of squares.

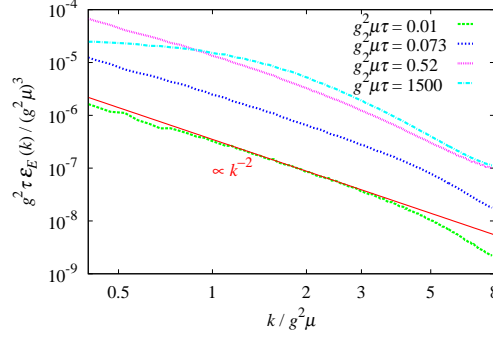


Fig. 4. Energy spectrum  $\tau \epsilon_E(k_\perp)$  at  $g^2 \mu \tau = 0.01, 0.073, 0.52$ , and  $1500$ . The transverse size is chosen as  $N = 300$  and the MV model parameter as  $g^2 \mu L = 120$ . The spectrum at  $g^2 \mu \tau = 0.01$  shows the perturbative scaling  $\epsilon_E(k_\perp) \propto k_\perp^{-2}$ . An ensemble average is taken over 30 configurations.

the asymptotic one within  $g^2 \mu \tau \sim 1$  and it hardly changes after that time. In fact the shape at  $g^2 \mu \tau = 0.52$  is already close to that at  $g^2 \mu \tau = 1500$  (where we stopped the simulation). Thanks to this, we do not show the results at any intermediate time between  $g^2 \mu \tau = 0.52$  and  $g^2 \mu \tau = 1500$  in order to keep the plot legible.

In later discussions in the section 5 we will perform a similar analysis in the longitudinal direction to find non-trivial asymptotic behavior of the spectral shapes.

## 4 Breaking the Boost Invariance

After this summary of the boost-invariant results, including the time evolution of the energy spectrum, let us proceed with the analysis of the instability with respect to  $\eta$ -dependent fluctuations. We will first confirm the existence of the instability in a similar setup as the one used in previous studies. For this purpose, we choose the initial fluctuations according to the prescription used in Refs. [43,44] and we fix the MV model parameter  $g^2 \mu$  in the same way as in the boost-invariant situation. We take the extent in the  $\eta$  direction to be  $L_\eta = 2$  units of rapidity and we use periodic boundary conditions for  $\eta$  as well as for transverse coordinates. We note that this extent covers roughly the mid-rapidity region where the boost-invariant plateau is expected, and therefore it is legitimate to have a boost-invariant background. That is, our parameter choice reads;

$$g^2 \mu a = \frac{120}{N} \quad (g = 2), \quad a_\eta = \frac{2.0}{N_\eta}, \quad (24)$$

and we perform calculations at various values of the transverse grid size  $N$  and the longitudinal grid size  $N_\eta$  later.

Introducing an arbitrary function  $f(\eta)$ , we can write the  $\eta$ -dependent chromo-electric fields in such a way that Gauss's law is satisfied by construction,

$$\delta E^i(x) = a_\eta^{-1} [f(\eta - a_\eta) - f(\eta)] \xi^i(\mathbf{x}_\perp) , \quad (25)$$

$$\delta E^\eta(x) = -f(\eta) \sum_{i=x,y} \left[ U_i^\dagger(x - \hat{i}) \xi^i(\mathbf{x}_\perp - \hat{i}) U_i(x - \hat{i}) - \xi^i(\mathbf{x}_\perp) \right] . \quad (26)$$

Before applying Eq. (26) we can also add  $\eta$ -dependent fluctuations in  $U_i$ . For the moment we will discuss the case with  $\delta E^i$  and  $\delta E^\eta$  only. Here the choice of  $\xi^i(\mathbf{x}_\perp)$  is arbitrary and we choose it as a random variable in the transverse plane, i.e.

$$\langle \xi^i(\mathbf{x}_\perp) \xi^j(\mathbf{x}'_\perp) \rangle = \delta^{ij} \delta^{(2)}(\mathbf{x}_\perp - \mathbf{x}'_\perp) . \quad (27)$$

It is important to note that  $\xi^i$  has the dimension of a momentum, which is obvious from the above equation. If all the dimensional quantities are scaled with the transverse spacing  $a$  as is the case in the numerical implementation,  $\xi^i$  scales as  $a^{-1}$ , which is artificial. The strength of the longitudinal disturbance should be given independently. To cancel this artificial  $a$  dependence, we use a dimensionless  $\bar{\xi}^i$  satisfying  $\langle \bar{\xi}^i(\mathbf{x}_\perp) \bar{\xi}^j(\mathbf{x}'_\perp) \rangle = \delta^{ij} \delta_{x,x'}$  (on the lattice) and make  $f(\eta)$  scale as  $N^{-1}$ , so that the fluctuations are proportional overall to  $(Na)^{-1} = L^{-1}$  which is a constant.

In the literature [43,44]  $f(\eta)$  is chosen as a random variable too containing all infrared and ultraviolet modes in the spectrum. Here, in order to study the instability behavior in a well-controlled situation, let us perturb the system with a single  $\eta$ -mode, and consider superposition of multiple modes only later<sup>5</sup>. Hence, we will adopt the following simple form for the moment<sup>6</sup>,

$$f(\eta) = \Delta \cos\left(\frac{2\pi\nu_0}{L_\eta}\eta\right) , \quad (28)$$

where  $L_\eta = N_\eta a_\eta$  is chosen to be 2 as we explained before and  $\Delta$  should scale as

$$\Delta = \frac{\Delta_0}{N} , \quad (29)$$

to make the fluctuations insensitive to the way we discretize the transverse plane. We will later fix  $\Delta_0$  and then vary  $N$  to study the (unphysical) dependence on the transverse grid size.

<sup>5</sup> It is legitimate to do so as long as the perturbations are small compared to the background field, so that their dynamics remains linear. After that, the different fluctuation modes will evolve non-linearly and mix. We will return to this point later.

<sup>6</sup> In this lattice parameterization of  $f(\eta)$ , the frequency  $\nu_0$  is an integer between  $-N_\eta/2$  and  $+N_\eta/2$ .

#### 4.1 Dependence on the transverse grid size $N$

Here we fix  $\nu_0 = 1$  in Eq. (28) because, as we will confirm later, this lowest non-zero mode leads to the fastest and strongest growth in the longitudinal pressure.

Figure 5 shows how the instability occurs in the longitudinal pressure  $P_L$  in the long-time run. The left-panel is the pressure multiplied by time ( $g^2\tau P_L$ ) in the unit of  $(g^2\mu)^3$ . We note that the plotted quantity is for  $\nu = \nu_0 = 1$  which maximizes the Fourier transform of  $\tau P_L$  (except for the zero mode  $\nu = 0$ ). That is, we define,

$$P_L(\nu) \equiv \frac{1}{L^2} \int d^2\mathbf{x}_\perp \frac{1}{L_\eta} \int_0^{L_\eta} d\eta P_L(\eta, \mathbf{x}_\perp) e^{i(2\pi\nu/L_\eta)\eta}, \quad (30)$$

which is complex valued in general<sup>7</sup>. We thus plot its modulus,  $|g^2\tau P_L(\nu = \nu_0)/(g^2\mu)^3|$ , in the left panel of Fig. 5 corresponding to an initial disturbance at  $\nu_0 = 1$  and  $\Delta_0 = 32 \times 10^{-5}$  in Eqs. (28) and (29) (i.e. we choose  $N = 32$  as a reference point and then  $\Delta = 10^{-5}$  for  $N = 32$ ). The horizontal axis represents  $\sqrt{g^2\mu\tau}$ , which is a natural variable in a longitudinally expanding geometry. Note that the Fourier transform  $P_L(\nu)$  at finite  $\nu$  is not a measurable quantity in experiments. Its real and imaginary parts both fluctuate from negative to positive values depending on the initial conditions and they would be vanishing if we compute an average without taking the modulus. Only the  $\nu = 0$  mode has a physical meaning as the longitudinal pressure. For our purpose of studying the instability, we can nevertheless consider  $\langle |P_L(\nu)| \rangle$  (i.e. we compute the modulus first, and we perform the average over initial conditions next) in order to confirm some known results reported previously [43,44]. In later discussions, we will also decompose the energy density into  $\nu$  components, which is a more well-defined quantity to see the instability.

From the left panel of Fig. 5, the exponential growth with the square root of proper time is obvious. The onset of the instability depends on the transverse size  $N$  but the instability slope is rather insensitive to  $N$ . With increasing  $N$ , the instability occurs earlier, and eventually the shift in this onset position saturates for  $N \approx 32$ . This means that the instability does not start earlier by increasing  $N$  further. So, we stop increasing  $N$  and conclude that simulations at  $N = 32$  are reasonably close to the continuum limit. In the right panel, we see how the fields, initially localized in the modes  $\nu_0 = 0$  (background field itself) and  $\nu_0 = \pm 1$  (perturbation), populate the higher  $\nu$  modes due to the non-linearities in the Yang-Mills equations. For a small perturbation, the amplitude in the higher modes decreases very fast (exponentially with  $\nu$ ),

<sup>7</sup> We note that  $\nu$  in our definition ranges from  $-N_\eta/2$  to  $N_\eta/2$  and the corresponding wave-number is  $k_\eta = 2\pi\nu/L_\eta$ .

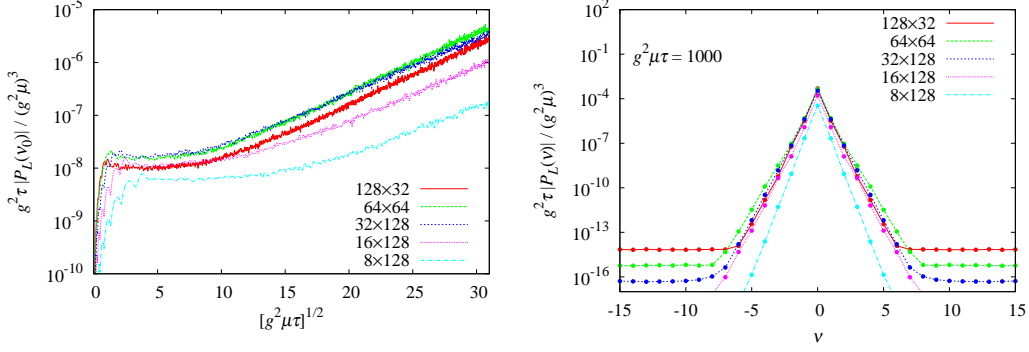


Fig. 5. Left: Longitudinal “pressure” at  $\nu = \nu_0$ , where  $\nu_0 = 1$  is chosen for the initial condition (28). The results are for  $N = 8, 16, 32, 64, 128$  in the transverse direction (from the top to the bottom) and  $N_\eta = 128$  fixed in the longitudinal direction (except for  $N_\eta = 64$  for  $N = 64$  and  $N_\eta = 32$  for  $N = 128$ ). The seed magnitude is  $\Delta = 10^{-5}$  for  $N = 32$ , i.e.  $\Delta_0 = 32 \times 10^{-5}$  in Eq. (29). An ensemble average is taken over 100 configurations. Right: Spectrum of the longitudinal “pressure” as a function of  $\nu$  at  $g^2 \mu \tau = 1000$  ( $\sqrt{g^2 \mu \tau} \approx 32$ ).

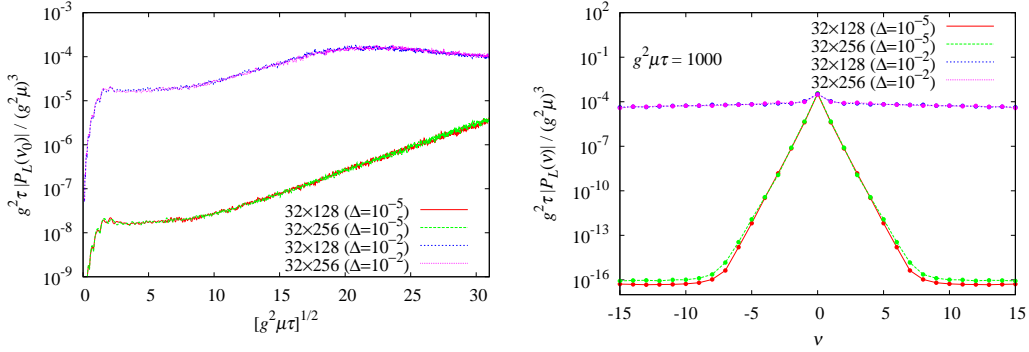


Fig. 6. Left: Longitudinal “pressure” at  $\nu = \nu_0 = 1$ . The results are for  $\Delta = 10^{-5}$  and  $N = 32$  fixed in the transverse direction and  $N_\eta = 128$  and  $N_\eta = 256$  in the longitudinal direction. An ensemble average is taken over 100 configurations. Right: Spectrum of the longitudinal “pressure” as a function of  $\nu$  at  $g^2 \mu \tau = 1000$ .

because in order to produce a field at a given  $\nu$ , one needs to multiply  $\nu$  seeds at  $\nu_0 = 1$ .

#### 4.2 Dependence on the longitudinal grid size $N_\eta$

Physical results must also not depend on how we discretize the longitudinal coordinate. In order to see the dependence on the longitudinal grid size, we make a plot in Fig. 6 in the same way as in Fig. 5, where we compare two longitudinal grid sizes that differ by a factor 2. As is clear from Fig. 6 we cannot find any sizable dependence on  $N_\eta$ , which means that our numerical calculations are safely free from lattice artifacts in the longitudinal direction.



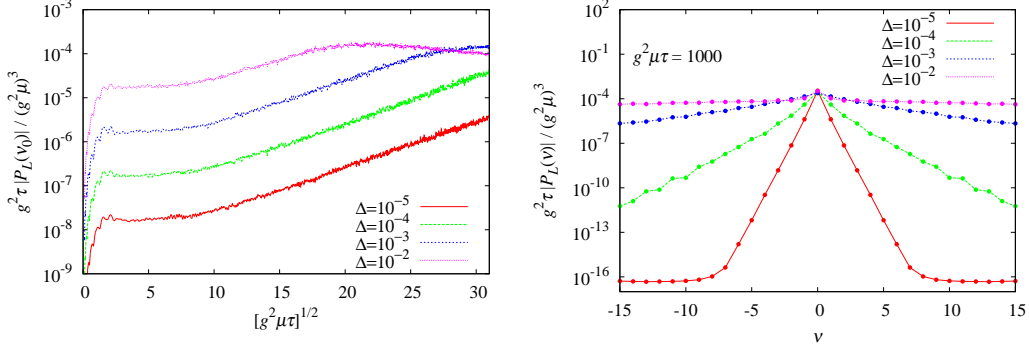


Fig. 7. Left: Longitudinal “pressure” at  $\nu = \nu_0 = 1$ . The results are for  $\Delta = 10^{-3}$ ,  $10^{-4}$ ,  $10^{-5}$  and a fixed lattice size  $32 \times 128$ . Right: Spectrum of the longitudinal “pressure” as a function of  $\nu$  at  $g^2 \mu \tau = 1000$ , which has a UV cutoff at  $\nu_{\max} = 64$  for the  $N_\eta = 128$  calculation.

The influence of  $N_\eta$  can be seen more clearly in the spectrum of  $|P_L(\nu)|$  shown in the right panel of Fig. 6. A different choice of  $N_\eta$  with fixed  $L_\eta = N_\eta a_\eta$  changes the UV cutoff (the spectrum ranges between  $-N_\eta/2$  and  $+N_\eta/2$ ): in the right panel of Fig. 6,  $\nu$  varies from  $-64$  to  $+64$  for the  $N_\eta = 128$  calculation and from  $-128$  to  $+128$  for the  $N_\eta = 256$  calculation. Since the seeds are at  $\nu = \nu_0 = 1$  in our initial condition, we naturally anticipate that the UV cutoff at  $\nu = N_\eta/2$  does not affect physical properties around  $\nu \sim \nu_0 \ll N_\eta/2$ .

One may think that the results for a larger seed amplitude  $\Delta = 10^{-2}$  in Fig. 6 could be sensitive to the choice of  $N_\eta$  because all the amplitudes in the spectrum are substantially larger and thus a change in  $N_\eta$  leading to a change in the UV cutoff may have an influence on the spectrum. We have also checked this and found that it is not the case. As is clear from Fig. 6, the difference between the results for  $32 \times 128$  with  $\Delta = 10^{-2}$  and that for  $32 \times 256$  with  $\Delta = 10^{-2}$  is almost invisible.

From all these results we can conclude that a value of  $N_\eta = 128$  is sufficiently large as long as  $\nu_0$  is set to be of order unity. If  $\nu_0$  takes a larger value, as we will see soon below, the spectral shape has a wider distribution and the UV cutoff at  $\nu = N_\eta/2$  could influence the results.

#### 4.3 Dependence on the magnitude $\Delta$ of the seed

In this subsection, we study the dependence on the seed magnitude  $\Delta$  of the longitudinal fluctuations in Eq. (28). In Fig. 7, we show some of numerical results for different values of  $\Delta$ . It is interesting that the results obviously scale as  $|P_L| \propto \Delta$  up to the point where the instability growth eventually saturates. This  $\Delta$  dependence is almost trivial, which suggests that the non-linear effects in terms of finite- $\nu$  modes are small unless the unstable modes substantially

develop at large  $g^2\mu\tau$ . One might have thought that any physical observables should be expanded in even powers of  $\Delta$  and thus  $|P_L(\nu_0)|$  should be proportional  $\Delta^2$  rather than  $\Delta$ . This is not the case because we took the modulus of complex  $P_L(\nu_0)$  before performing the average over initial conditions, thus preventing the linear term in  $\Delta$  from vanishing.

We can also notice from the right panel of Fig. 7 that, once the instability at  $\nu = \nu_0$  gets saturated, the mode at  $\nu = \nu_0$  stops growing but the spectrum spreads quickly to higher  $\nu$ -modes. Once this happens, the scaling property with  $\Delta$  is lost. Actually the amplitude of the  $\nu = \nu_0$  mode reaches one third of the zero-mode amplitude (for  $\Delta = 10^{-2}$  results at  $g^2\mu\tau = 1000$ ) before this saturation occurs. Then the non-linearities or self-interaction effects cannot be neglected any longer.

#### 4.4 *Dependence on the initial seed wave-number $\nu_0$*

Now we investigate the  $\nu_0$ -dependence of the instability behavior. First, we have chosen three different  $\nu_0$ 's as  $\nu_0 = 1, 5$ , and  $10$  to uncover the general trend. Then we study a more general case, that consists in a superposition of these initial wave-numbers.

The figure 8 shows the numerical results. It is clear from the figure that the onset of the instability is delayed for larger  $\nu_0$ . This is naturally understandable from the kinetic term for finite- $\nu$  modes. The (positive) kinetic term generally tends to stabilize the system, and so the (negative) term responsible for the instability is overwhelmed if  $\nu$  is large enough. For dimensional reasons, however, this kinetic term for the finite- $\nu$  modes is of the form  $\nu^2/\tau^2$ , and therefore it decreases with time. In contrast, the negative term that generates the instability has a constant coefficient of order unity – therefore, it dominates over the kinetic term at sufficiently large time. In other words, the kinetic term in  $\nu^2/\tau^2$  only delays the start of the instability by a time proportional to  $\nu$ . We can confirm qualitatively this interpretation from Fig. 8. The growth appears to start around  $\sqrt{g^2\mu\tau} \sim 9.5, 21, 30$  for  $\nu_0 = 1, 5, 10$ , respectively, and the starting times are indeed ordered proportionally to  $\nu_0$ .

The spectral shape shown in the right panel of Fig. 8 looks discontinuous for  $\nu_0 = 5$  and  $10$ , but this is a trivial artifact of the fact that our initial seed contains a single  $\nu_0$  mode. Indeed, the non-linear couplings in the Yang-Mills equations can only produce linear combinations with integer coefficients of the frequencies present in the initial condition. For instance, with  $\nu_0 = 5$ , only modes with  $\nu$  a multiple of  $5$  can be produced by the non-linear evolution. The fact that the amplitude of these higher harmonics is suppressed compared to the amplitude of the base frequency  $\nu_0$  is a good indication that we are still

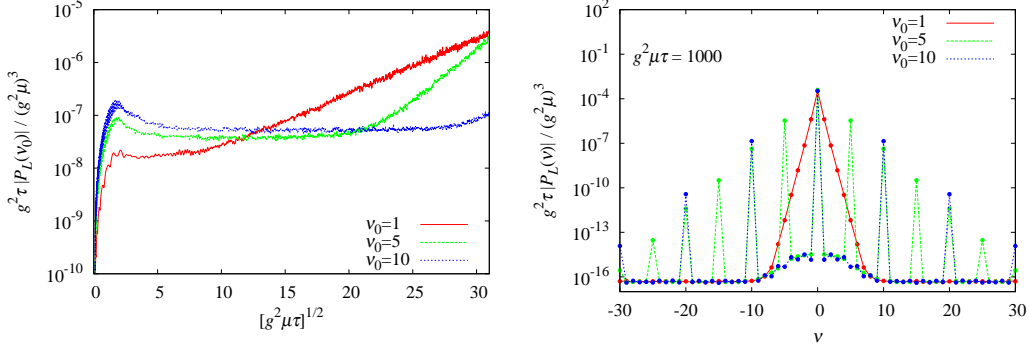


Fig. 8. Left: Longitudinal “pressure” at  $\nu = \nu_0$  with  $\nu_0 = 1, 5$ , and  $10$  in the initial condition (28). The lattice size  $32 \times 128$  is fixed and the seed amplitude is  $\Delta = 10^{-5}$ . Right: Spectrum of the longitudinal “pressure” as a function of  $\nu$  at  $g^2 \mu \tau = 1000$ .

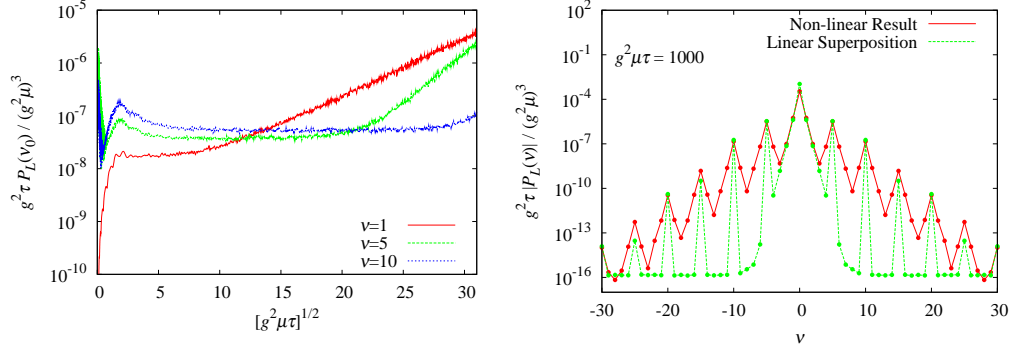


Fig. 9. Left: Longitudinal “pressure” at  $\nu = 1, 5$ , and  $10$  with the initial condition given as a superposition (31). Right: Spectrum of the longitudinal “pressure” as a function of  $\nu$  at  $g^2 \mu \tau = 1000$ . The solid line represents the results from the non-linear evolution with the initial condition given as a superposition, while the dotted one is a simple linear superposition of the results shown in Fig. 8.

in a regime where the non-linearities are rather small.

We can also see that the non-linear effects are certainly present but not very large by repeating the above calculation with an initial condition given as a superposition of three modes, namely,

$$f(\eta) = \Delta \sum_i \cos\left(\frac{2\pi\nu_0^{(i)}}{L_\eta} \eta\right) \quad (31)$$

with  $\nu_0^{(1)} = 1$ ,  $\nu_0^{(2)} = 5$ ,  $\nu_0^{(3)} = 10$ , instead of the single-mode fluctuation of Eq. (28) with  $\nu_0 = 1$ ,  $\nu_0 = 5$ ,  $\nu_0 = 10$  individually. If the non-linearity is significant, the results should not be a simple superposition of the individual calculation. In view of Fig. 9, however, we can see only small deviations from the individual results shown in Fig. 8 at  $g^2 \mu \tau = 1000$ . This is an important observation because the initial fluctuations in reality should have some continuous spectral distribution (see Ref. [50] for instance) and we simplified our analysis by considering the special case of a single-mode fluctuation. As long

as the non-linearity is a minor effect, we can just add up the single-mode outputs in order to get approximate results for general initial spectra.

Although they are several orders of magnitude smaller at  $g^2\mu\tau = 1000$ , we see that higher harmonics mixing the three  $\nu_0$ 's are enhanced by non-linear effects in the right panel of Fig. 9. For instance, the amplitude of the mode  $\nu = 21$  is much larger than the sum of the amplitudes at  $\nu = 21$  for the three seeds considered in isolation. Indeed, when the seed  $\nu_0 = 1$  is alone for example, the mode  $\nu = 21$  is produced only after 20 interactions, which explains why it is totally negligible. Furthermore, the seeds  $\nu_0 = 5$  or 10 can never lead to  $\nu = 21$  by themselves. When the three seeds are superposed in the initial condition, 21 can be reached more efficiently as  $10 + 10 + 1$ , i.e. with 2 interactions only.

Apart from small non-linear effects, it is certainly true that the smallness of the field fluctuations we have considered gives a justification for our simplified, single mode, analysis. However, at the same time, thermalization is hardly expected to occur in these circumstances, precisely because in this regime the interaction effects are small. In realistic conditions, the parameter  $\Delta$  that controls the fluctuations is related to the strong coupling  $\alpha_s$ , and therefore it could be larger than  $\Delta_0 = 10^{-5}$  that we have considered here. As a consequence, we expect that the non-linearities would start much sooner and be much more important in applications of this framework to actual heavy-ion collisions. The study with such large  $\Delta$  is beyond our current scope because a large  $\Delta$  requires full information on quantum fluctuations and needs appropriate renormalization procedures, which is technically involved [59].

## 5 Time Evolution of the Longitudinal Spectrum

In spite of the instability the zero-mode is still dominant among all the modes in  $P_L(\nu)$ . With an initial condition that contains a single mode as in Eq. (28), the  $\nu = \nu_0 = 1$  mode is the second largest, which is obvious from the spectrum shown in the right panel of Fig. 5. Moreover, the spectrum is spreading into higher wave-numbers as the time elapses. In this section, we shall discuss the scaling property of the energy spectrum with respect to the frequency  $\nu$ , and show that it possibly displays also a Kolmogorov's turbulent spectrum. A turbulent spectrum has already been reported in the context of the QCD plasma instability [8,18], but these results with the power  $\simeq -2$  instead of  $-5/3$  are in conflict with Kolmogorov's wave turbulence. On the other hand, the study performed in Ref. [60] has shown that a Kolmogorov spectrum appears due to instabilities in Yang-Mills theory, for a fixed-volume system. Therefore, it is still worth addressing the turbulent spectrum in the present Glasma simulation, that has longitudinal expansion. This is because the Glasma system is expanding along the beam axis, which tends to tame the turbulences and

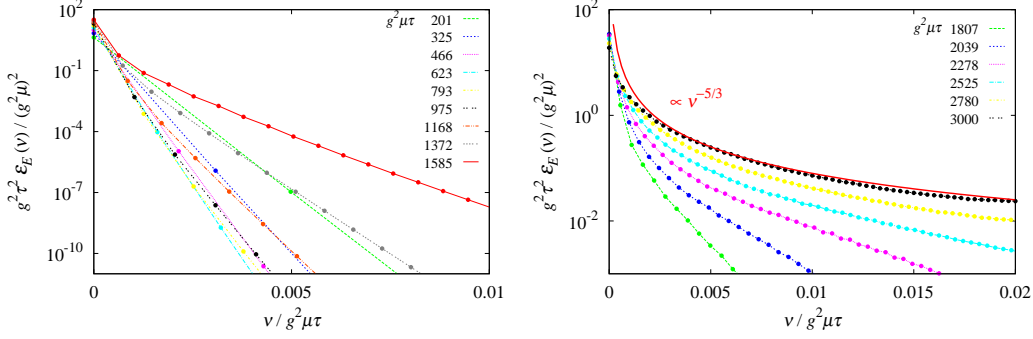


Fig. 10. Time evolution of the chromo-electric energy density as a function of the scaled longitudinal wave-number  $\nu/(g^2\mu\tau)$ . The lattice size is  $32 \times 128$  and the seed is  $\Delta = 10^{-5}$ . Left: Results at early times up to  $g^2\mu\tau \sim 1500$ . Note that the horizontal axis is not logarithmic and also that the vertical axis is for not  $\tau\epsilon_E(\nu)$  but  $\tau^2\epsilon_E(\nu)$  (see the text for details). Right: Results at later times up to  $g^2\mu\tau = 3000$ .

to delay the isotropization or thermalization in general. It is thus non-trivial whether the universal scaling still holds or not in the expanding system. Besides, our description of the Glasma evolution is purely classical and the precise relationship between the Glasma instability and the QCD plasma instability is not fully understood yet.

Two plots in Fig. 10 show the longitudinal energy spectrum (for the chromo-electric part only), that is, the energy density decomposed in terms of the longitudinal wave-number  $\nu$  as

$$\epsilon_E = \int \frac{d\nu}{2\pi} \epsilon_E(\nu) \quad (32)$$

with

$$\epsilon_E(\nu) \equiv \left\langle \text{tr} \left[ E^{\eta a}(-\nu) E^{\eta a}(\nu) + \tau^{-2} \left( E^{ia}(-\nu) E^{ia}(\nu) \right) \right] \right\rangle. \quad (33)$$

(The transverse momentum  $\mathbf{k}_\perp$  of the fields is integrated over.) The question is then what kind of scaling spectrum we can expect for  $\epsilon_E(\nu)$  at later times. For this purpose, we consider three characteristic quantities; the wave-number, the Fourier decomposed energy, and the rate of energy flow in  $\nu$ -space (denoted by  $\psi$  below). The wave-number  $\nu$  itself is, however, dimensionless and it seems difficult to cope with the dimensional matching argument by Kolmogorov. We propose that one should use a scaled variable  $\nu/(c\tau)$  instead of  $\nu$ , in the case of an expanding geometry. This is because  $c\tau\eta$  is approximately equal to the longitudinal coordinate  $z$  if  $\eta$  is small enough, and  $\nu/(c\tau)$  is approximately equal to the momentum  $p_z$ . Then, the dimension of the scaled wave-number is  $[\nu/c\tau] = l^{-1}$ . We note that the integration variable in the decomposition (32) should also be  $\nu/c\tau$  for this scaling analysis, which means that the relevant energy density per mode should be  $c\tau\epsilon_E(\nu)$ . This in addition should be multiplied by the expanding length  $c\tau$ . Therefore, the dimensions of the three

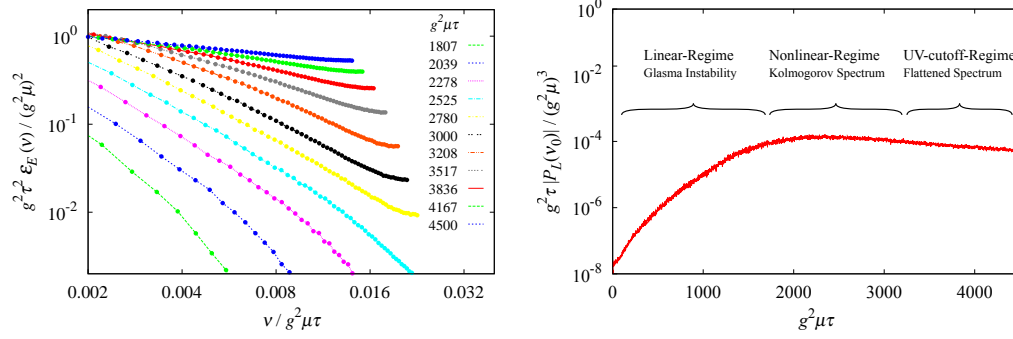


Fig. 11. Time evolution of the chromo-electric energy density as a function of the scaled longitudinal wave-number  $\nu/(g^2\mu\tau)$  up to  $g^2\mu\tau = 4500$ . Left: Results including later time spectra. The horizontal axis is logarithmic to make it evident how the power-law spectrum spreads. Right: Longitudinal “pressure” with three regimes identified schematically.

relevant quantities are

$$[\nu/c\tau] = l^{-1}, \quad [V_\perp(c\tau)^2\epsilon_E(\nu)] = l^3t^{-2}, \quad [\psi] = l^2t^{-3}, \quad (34)$$

which are identical to the standard analysis of Kolmogorov’s spectrum. Provided that  $V_\perp(c\tau)^2\epsilon_E(\nu)$  is expressed in a form of  $(\nu/c\tau)^\alpha(\psi)^\beta$ , we can fix  $\alpha$  and  $\beta$  uniquely from the dimensions and thus expect the Kolmogorov scaling, that is,  $\tau^2\epsilon_E(\nu) \propto (\nu/\tau)^{-5/3}$ . In fact we can confirm this scaling property asymptotically from the right panel of Fig. 10.

One might be wondering what the fate of the power-law spectrum should be at even later times. We understand from Fig. 11 that the Glasma time evolution in the present MV-model simulation has three stages; the linear regime, the non-linear regime, and the UV-cutoff regime. In the linear regime the unstable modes grow up and the non-linear effects are still minor. When the amplitudes of  $\nu \neq 0$  modes become so large that the non-linearities can affect the time evolution, the instability stops, as shown in the right panel of Fig. 11, and the non-Abelianization occurs [7,14]. Because non-linearities are no longer negligible in this regime, the energy cascade due to non-linearities is naturally expected, which would lead to the Kolmogorov-type spectrum. Eventually, as the turbulence decays into higher UV modes, the UV-cutoff effect flattens the whole spectrum as plotted in Fig. 11 up to  $g^2\mu\tau = 4500$ .

To the best of our knowledge the present work is the first to exhibit a Kolmogorov spectrum from the Glasma time evolution. Our results imply that the framework of the Glasma, in terms of classical variables together with  $\eta$ -dependent fluctuations, may encompass a rich physics contents including the QCD plasma instability.

Here, as a final remark in this section, we draw attention to related works

in analogous systems. In the context of an ultra-cold gas, the Kolmogorov spectrum has been obtained as a solution of the Gross-Pitaevskii equation (GPE), which is a classical equation of motion like the Glasma equations [61]. The calculational procedure by means of the GPE is similar to the Glasma simulation, but in that case the microscopic mechanism of the energy flow is understood in terms of the vortex dynamics. In future studies on the Glasma dynamics, it will be important to clarify the structure of the energy flow, and it would be very interesting to see whether the so-called non-thermal fixed point [62] appears in the strongly correlated Yang-Mills theory and Glasma. Indeed, a possible deviation in the power could be expected in Yang-Mills theory by non-perturbative resummations [63].

## 6 Summary and Outlook

In this paper we investigated the time evolution of the classical equations of motion in the  $SU(2)$  pure Yang-Mills theory, especially in the framework of the Glasma or the McLerran-Venugopalan model in  $(3+1)$  dimensions. Our emphasis has been put on the systematic study of the instability behavior that occurs in fluctuations with respect to the space-time rapidity  $\eta$  when the initial conditions break boost invariance.

Computing the longitudinal pressure component at non-zero wave-number  $\nu$ , that is a conjugate of  $\eta$ , we have numerically confirmed the Glasma instability that had been found in preceding works [43,44]. We carefully checked the system size dependence of the instability to conclude that the Glasma instability is a robust consequence from  $\eta$ -dependent disturbances and is not sensitive to how the transverse and longitudinal coordinates are discretized. Hence, the Glasma instability is certainly a physically well-defined phenomenon. At the same time, however, this means that taking the continuum limit does not help with an earlier onset of the instability. The typical time scales we found for the Glasma instability is of order of hundreds in terms of  $g^2\mu\tau$ , which is arguably too slow for being useful in heavy ion collisions. One should however keep in mind that the seeds we have used in this numerical study are very small compared to the Glasma fields, while in a realistic situation they are suppressed at most by a power of the strong coupling constant. There may also be a chance that the non-linear effects could more or less accelerate the instability. We compared two results for the spectral distribution, one from the superposition of individual calculations with the initial condition that is given by a different wave-number  $\nu_0$ , and the other from a single calculation with the initial condition that contains all  $\nu_0$ 's. We could observe the non-linear effects in our numerical results, which would not affect the instability behavior substantially, however, as long as the instability seed  $\Delta$  is reasonably small.



We have decomposed the energy density into Fourier modes to see how the low wave-number modes cascade toward higher wave-number modes due to non-linearity in the equations of motion. Our motivation to do so is to examine whether the so-called Kolmogorov's scaling can appear in the turbulent system described by the Yang-Mills theory put in an expanding geometry. In contrast to the boost-invariant case, a Kolmogorov-type scaling behavior in the energy spectrum as a function of the longitudinal wave-number  $\nu$  may appear when the boost invariance is broken by the initial fluctuations. In this case, the violation of boost invariance increases with time due to instability, but the  $\nu = 0$  mode remains very large compared to the other  $\nu \neq 0$  modes, which enables us to regard the  $\nu = 0$  mode as the source for the energy injection. Then, we could clearly observe that the energy spectra approach an asymptotic form that shows the Kolmogorov's scaling with the power  $-5/3 \simeq -1.67$ . As far as we know, our work is the first example that exhibits the Kolmogorov-type scaling law in the expanding systems. Although it is difficult to find any indication that the system indeed becomes isotropic and thermalized in our simulation, the confirmation of the Kolmogorov-type spectra is a promising signal for the general tendency heading for thermalization.

There remain very interesting questions to be investigated in the future. In order to unveil the microscopic mechanism for the instability, it would be very useful to make approximations on the classical equations of motion in such a way that the analytical treatment could be feasible. For instance, as we have confirmed, the instability mostly lies in the linear regime as long as its magnitude specified by  $\Delta$  is small enough. Therefore the linearization of the equations of motion in terms of fluctuating fields on top of the boost-invariant CGC background should correctly describe the instability in early times. In this work we did not exploit such a comparison between the numerical output and the analytical result from the linearized equations. This is because it is not quite efficient to linearize the equations of motion given in terms of the lattice variables. The linearization is of course possible, but it would eventually be reduced to similar calculations in the continuum formulation. Then, it would make much more sense to make a comparison between the numerical and analytical results that are both formulated in the continuum variables. We have already executed test programs to make sure if the numerical results from the Glasma simulations are consistent with each other, given they are written in terms of lattice and continuum variables. We will report on this analysis elsewhere.

It is also an intriguing question to look for a link between Kolmogorov's turbulent spectrum and the chaotic behavior generally seen in the solution of the classical Yang-Mills equations. This problem may have some relevance for a deeper understanding of the microscopic description of the entropy generating process and how the thermalization is achieved at all. The time evolution of the Glasma and its physics contents deserve much more investigations in the



future.

## Acknowledgments

We would like to thank Kevin Dusling, Tuomas Lappi, and Raju Venugopalan for discussions. This work has been supported in part by JSPS Japan-France Integrated Action Program (SAKURA). F.G. thanks the Yukawa Institute for Theoretical Physics, where part of this work has been done, for its hospitality and support.

## References

- [1] P. F. Kolb and R. Rapp, “Transverse flow and hadrochemistry in Au+Au collisions at  $\sqrt{s_{NN}} = 200$  GeV,” *Phys. Rev.* **C67** (2003) 044903, [arXiv:hep-ph/0210222](#) [hep-ph].
- [2] U. W. Heinz, “Thermalization at RHIC,” *AIP Conf. Proc.* **739** (2005) 163–180, [arXiv:nuc1-th/0407067](#) [nuc1-th].
- [3] R. Baier, A. H. Mueller, D. Schiff, and D. T. Son, “‘Bottom-up’ thermalization in heavy ion collisions,” *Phys. Lett.* **B502** (2001) 51–58, [arXiv:hep-ph/0009237](#).
- [4] Y. V. Kovchegov, “Can thermalization in heavy ion collisions be described by QCD diagrams?,” *Nucl. Phys.* **A762** (2005) 298–325, [arXiv:hep-ph/0503038](#).
- [5] P. B. Arnold, J. Lenaghan, and G. D. Moore, “QCD plasma instabilities and bottom up thermalization,” *JHEP* **0308** (2003) 002, [arXiv:hep-ph/0307325](#) [hep-ph]. Erratum added online, sep/29/2004.
- [6] P. B. Arnold, J. Lenaghan, G. D. Moore, and L. G. Yaffe, “Apparent thermalization due to plasma instabilities in quark-gluon plasma,” *Phys. Rev. Lett.* **94** (2005) 072302, [arXiv:nuc1-th/0409068](#) [nuc1-th].
- [7] P. B. Arnold, G. D. Moore, and L. G. Yaffe, “The Fate of non-Abelian plasma instabilities in 3+1 dimensions,” *Phys. Rev.* **D72** (2005) 054003, [arXiv:hep-ph/0505212](#) [hep-ph].
- [8] P. B. Arnold and G. D. Moore, “QCD plasma instabilities: The NonAbelian cascade,” *Phys. Rev.* **D73** (2006) 025006, [arXiv:hep-ph/0509206](#) [hep-ph].
- [9] J. Randrup and S. Mrowczynski, “Chromodynamic Weibel instabilities in relativistic nuclear collisions,” *Phys. Rev.* **C68** (2003) 034909, [arXiv:nuc1-th/0303021](#).

- [10] S. Mrowczynski, “Instabilities driven equilibration of the quark-gluon plasma,” *Acta Phys. Polon.* **B37** (2006) 427–454, [arXiv:hep-ph/0511052](#).
- [11] A. Dumitru, Y. Nara, and M. Strickland, “Ultraviolet avalanche in anisotropic non-Abelian plasmas,” *Phys. Rev.* **D75** (2007) 025016, [arXiv:hep-ph/0604149](#) [hep-ph].
- [12] J. Berges, D. Gelfand, S. Scheffler, and D. Sexty, “Simulating plasma instabilities in SU(3) gauge theory,” *Phys. Lett.* **B677** (2009) 210–213, [arXiv:0812.3859](#) [hep-ph].
- [13] D. Bodeker, “The impact of QCD plasma instabilities on bottom-up thermalization,” *JHEP* **0510** (2005) 092, [arXiv:hep-ph/0508223](#) [hep-ph].
- [14] A. Rebhan, P. Romatschke, and M. Strickland, “Hard-loop dynamics of non-Abelian plasma instabilities,” *Phys. Rev. Lett.* **94** (2005) 102303, [arXiv:hep-ph/0412016](#).
- [15] A. Rebhan, P. Romatschke, and M. Strickland, “Dynamics of quark-gluon plasma instabilities in discretized hard-loop approximation,” *JHEP* **09** (2005) 041, [arXiv:hep-ph/0505261](#).
- [16] P. Romatschke and A. Rebhan, “Plasma instabilities in an anisotropically expanding geometry,” *Phys. Rev. Lett.* **97** (2006) 252301, [arXiv:hep-ph/0605064](#).
- [17] A. Rebhan, M. Strickland, and M. Attems, “Instabilities of an anisotropically expanding non-Abelian plasma: 1D+3V discretized hard-loop simulations,” *Phys. Rev.* **D78** (2008) 045023, [arXiv:0802.1714](#) [hep-ph].
- [18] A. Ipp, A. Rebhan, and M. Strickland, “Non-Abelian plasma instabilities: SU(3) vs. SU(2),” [arXiv:1012.0298](#) [hep-ph].
- [19] B. Muller and A. Trayanov, “Deterministic chaos in nonAbelian lattice gauge theory,” *Phys. Rev. Lett.* **68** (1992) 3387–3390.
- [20] T. S. Biro, C. Gong, and B. Muller, “Lyapunov exponent and plasmon damping rate in nonabelian gauge theories,” *Phys. Rev.* **D52** (1995) 1260–1266, [arXiv:hep-ph/9409392](#).
- [21] T. Kunihiro *et al.*, “Chaotic behavior in classical Yang-Mills dynamics,” *Phys. Rev.* **D82** (2010) 114015, [arXiv:1008.1156](#) [hep-ph].
- [22] A. Nishiyama and A. Ohnishi, “Entropy production in gluodynamics in temporal axial gauge in 2+1 dimensions,” *Prog. Theor. Phys.* **125** (2011) 775–795, [arXiv:1011.4750](#) [nucl-th].
- [23] P. M. Chesler and L. G. Yaffe, “Horizon formation and far-from-equilibrium isotropization in supersymmetric Yang-Mills plasma,” *Phys. Rev. Lett.* **102** (2009) 211601, [arXiv:0812.2053](#) [hep-th].
- [24] P. M. Chesler and L. G. Yaffe, “Boost invariant flow, black hole formation, and far-from-equilibrium dynamics in  $N = 4$  supersymmetric Yang-Mills theory,” *Phys. Rev.* **D82** (2010) 026006, [arXiv:0906.4426](#) [hep-th].

- [25] Y. V. Kovchegov and S. Lin, “Toward thermalization in heavy ion collisions at strong coupling,” *JHEP* **03** (2010) 057, [arXiv:0911.4707 \[hep-th\]](#).
- [26] V. Balasubramanian *et al.*, “Thermalization of strongly coupled field theories,” [arXiv:1012.4753 \[hep-th\]](#).
- [27] F. Gelis, T. Lappi, and R. Venugopalan, “High energy scattering in Quantum Chromodynamics,” *Int.J.Mod.Phys.* **E16** (2007) 2595–2637, [arXiv:0708.0047 \[hep-ph\]](#).
- [28] F. Gelis, E. Iancu, J. Jalilian-Marian, and R. Venugopalan, “The Color Glass Condensate,” [arXiv:1002.0333 \[hep-ph\]](#). \* Temporary entry \*.
- [29] L. D. McLerran and R. Venugopalan, “Computing quark and gluon distribution functions for very large nuclei,” *Phys. Rev.* **D49** (1994) 2233–2241, [arXiv:hep-ph/9309289](#).
- [30] L. D. McLerran and R. Venugopalan, “Gluon distribution functions for very large nuclei at small transverse momentum,” *Phys. Rev.* **D49** (1994) 3352–3355, [arXiv:hep-ph/9311205](#).
- [31] L. D. McLerran and R. Venugopalan, “Fock space distributions, structure functions, higher twists and small x,” *Phys. Rev.* **D59** (1999) 094002, [arXiv:hep-ph/9809427](#).
- [32] A. Kovner, L. D. McLerran, and H. Weigert, “Gluon production from nonAbelian Weizsacker-Williams fields in nucleus-nucleus collisions,” *Phys. Rev.* **D52** (1995) 6231–6237, [arXiv:hep-ph/9502289](#).
- [33] A. Kovner, L. D. McLerran, and H. Weigert, “Gluon production at high transverse momentum in the McLerran-Venugopalan model of nuclear structure functions,” *Phys. Rev.* **D52** (1995) 3809–3814, [arXiv:hep-ph/9505320](#).
- [34] D. Son, “Semiclassical approach for multiparticle production in scalar theories,” *Nucl. Phys.* **B477** (1996) 378–406, [arXiv:hep-ph/9505338 \[hep-ph\]](#).
- [35] A. Mueller and D. Son, “On the equivalence between the Boltzmann equation and classical field theory at large occupation numbers,” *Phys. Lett.* **B582** (2004) 279–287, [arXiv:hep-ph/0212198 \[hep-ph\]](#).
- [36] A. Krasnitz and R. Venugopalan, “Non-perturbative computation of gluon mini-jet production in nuclear collisions at very high energies,” *Nucl. Phys.* **B557** (1999) 237, [arXiv:hep-ph/9809433](#).
- [37] A. Krasnitz and R. Venugopalan, “The initial energy density of gluons produced in very high energy nuclear collisions,” *Phys. Rev. Lett.* **84** (2000) 4309–4312, [arXiv:hep-ph/9909203](#).
- [38] A. Krasnitz and R. Venugopalan, “The initial gluon multiplicity in heavy ion collisions,” *Phys. Rev. Lett.* **86** (2001) 1717–1720, [arXiv:hep-ph/0007108](#).

- [39] T. Lappi, “Production of gluons in the classical field model for heavy ion collisions,” *Phys. Rev.* **C67** (2003) 054903, [arXiv:hep-ph/0303076](#).
- [40] T. Lappi and L. McLerran, “Some features of the glasma,” *Nucl. Phys.* **A772** (2006) 200–212, [arXiv:hep-ph/0602189](#).
- [41] A. Dumitru, F. Gelis, L. McLerran, and R. Venugopalan, “Glasma flux tubes and the near side ridge phenomenon at RHIC,” *Nucl. Phys.* **A810** (2008) 91–108, [arXiv:0804.3858 \[hep-ph\]](#).
- [42] K. Dusling, F. Gelis, T. Lappi, and R. Venugopalan, “Long range two-particle rapidity correlations in A+A collisions from high energy QCD evolution,” *Nucl. Phys.* **A836** (2010) 159–182, [arXiv:0911.2720 \[hep-ph\]](#).
- [43] P. Romatschke and R. Venugopalan, “Collective non-Abelian instabilities in a melting color glass condensate,” *Phys. Rev. Lett.* **96** (2006) 062302, [arXiv:hep-ph/0510121](#).
- [44] P. Romatschke and R. Venugopalan, “The unstable Glasma,” *Phys. Rev.* **D74** (2006) 045011, [arXiv:hep-ph/0605045](#).
- [45] K. Fukushima, “Initial fields and instability in the classical model of the heavy-ion collision,” *Phys. Rev.* **C76** (2007) 021902, [arXiv:0704.3625 \[hep-ph\]](#).
- [46] K. Fukushima, “Erratum: Initial fields and instability in the classical model of the heavy-ion collision,” [arXiv:0711.2634 \[hep-ph\]](#).
- [47] H. Fujii and K. Itakura, “Expanding color flux tubes and instabilities,” *Nucl. Phys.* **A809** (2008) 88–109, [arXiv:0803.0410 \[hep-ph\]](#).
- [48] H. Fujii, K. Itakura, and A. Iwazaki, “Instabilities in non-expanding glasma,” *Nucl. Phys.* **A828** (2009) 178–190, [arXiv:0903.2930 \[hep-ph\]](#).
- [49] K. Dusling, T. Epelbaum, F. Gelis, and R. Venugopalan, “Role of quantum fluctuations in a system with strong fields: Onset of hydrodynamical flow,” *Nucl. Phys.* **A850** (2011) 69–109, [arXiv:1009.4363 \[hep-ph\]](#).
- [50] K. Fukushima, F. Gelis, and L. McLerran, “Initial Singularity of the Little Bang,” *Nucl. Phys.* **A786** (2007) 107–130, [arXiv:hep-ph/0610416 \[hep-ph\]](#).
- [51] F. Gelis and R. Venugopalan, “Particle production in field theories coupled to strong external sources,” *Nucl. Phys.* **A776** (2006) 135–171, [arXiv:hep-ph/0601209 \[hep-ph\]](#).
- [52] F. Gelis and R. Venugopalan, “Particle production in field theories coupled to strong external sources. II. Generating functions,” *Nucl. Phys.* **A779** (2006) 177–196, [arXiv:hep-ph/0605246 \[hep-ph\]](#).
- [53] F. Gelis, S. Jeon, and R. Venugopalan, “How particles emerge from decaying classical fields in heavy ion collisions: Towards a kinetic description of the Glasma,” *Nucl. Phys.* **A817** (2009) 61–89, [arXiv:0706.3775 \[hep-ph\]](#).

- [54] T. Lappi, “Energy density of the glasma,” *Phys. Lett.* **B643** (2006) 11–16, [arXiv:hep-ph/0606207](#).
- [55] E. Iancu, K. Itakura, and L. McLerran, “A Gaussian effective theory for gluon saturation,” *Nucl. Phys.* **A724** (2003) 181–222, [arXiv:hep-ph/0212123](#).
- [56] A. Krasnitz, Y. Nara, and R. Venugopalan, “Gluon production in the color glass condensate model of collisions of ultrarelativistic finite nuclei,” *Nucl. Phys.* **A717** (2003) 268–290, [arXiv:hep-ph/0209269](#) [[hep-ph](#)].
- [57] A. Krasnitz, Y. Nara, and R. Venugopalan, “Classical gluodynamics of high-energy nuclear collisions: An Erratum and an update,” *Nucl. Phys.* **A727** (2003) 427–436, [arXiv:hep-ph/0305112](#) [[hep-ph](#)].
- [58] H. Fujii, K. Fukushima, and Y. Hidaka, “Initial energy density and gluon distribution from the Glasma in heavy-ion collisions,” *Phys. Rev.* **C79** (2009) 024909, [arXiv:0811.0437](#) [[hep-ph](#)].
- [59] K. Dusling, F. Gelis, and R. Venugopalan, “The initial spectrum of fluctuations in the little bang,” [arXiv:1106.3927](#) [[nucl-th](#)]. \* Temporary entry \*.
- [60] J. Berges, S. Scheffler, and D. Sexty, “Turbulence in nonabelian gauge theory,” *Phys. Lett.* **B681** (2009) 362–366, [arXiv:0811.4293](#) [[hep-ph](#)].
- [61] B. Nowak, D. Sexty, and T. Gasenzer, “Quantum turbulence in an ultracold Bose gas,” [arXiv:1012.4437](#) [[cond-mat.quant-gas](#)]. \* Temporary entry \*.
- [62] J. Berges, A. Rothkopf, and J. Schmidt, “Non-thermal fixed points: Effective weak-coupling for strongly correlated systems far from equilibrium,” *Phys. Rev. Lett.* **101** (2008) 041603, [arXiv:0803.0131](#) [[hep-ph](#)].
- [63] M. Carrington and A. Rebhan, “Perturbative and nonperturbative Kolmogorov turbulence in a Gluon Plasma,” [arXiv:1011.0393](#) [[hep-ph](#)].